nature communications

Article

https://doi.org/10.1038/s41467-024-55792-9

Deep mantle earthquakes linked to CO_2 degassing at the Mid-Atlantic Ridge

Received: 23 February 2023

Accepted: 30 December 2024

Published online: 10 January 2025

Check for updates

Zhiteng Yu[1,2,3] ✉, Satish C. Singh[3] ✉, Cédric Hamelin[4], Léa Grenet[2], Marcia Maia[2], Anne Briais[2], Lorenzo Petracchini[5] & Daniele Brunelli[5,6]

Volatiles (CO_2, H_2O) play a fundamental role in mantle melting beneath ocean spreading centers, but what role they play during the melt migration remains unknown. Using seismological data recorded by ocean-bottom seismometers, here we report the presence of deep earthquakes at 10–20 km depth in the mantle along the Mid-Atlantic Ridge axis, much below the brittle-ductile boundary. Syntheses of regional basaltic rock samples and their geochemical analyses indicate the presence of an abnormally high quantity of CO_2 (~0.4–3.0 wt%) in the primary melts. As the degassing of a high concentration of dissolved CO_2 produces volume change, we suggest that deep earthquakes in the mantle result from the degassing of CO_2. The large concentration of CO_2 in the primitive melt will influence the presence of melt beneath the lithosphere-asthenosphere boundary at sub-solidus temperatures.

Oceanic crust is formed by melt derived from the mantle at oceanic spreading centers. A small amount of melting initiates at ~150–300 km depths in the presence of volatiles (CO_2, H_2O)[1–4], but extensive dry melting commences at 60–70 km depths, driven by mantle upwelling as two diverging plates move apart[5–9]. Although partial melting occurs in a wide zone at depth[1], the melt is focused in a narrow zone beneath the ridge axis as it migrates upward and interacts with the host rocks. However, we have no clear understanding of how these melts migrate to the surface, especially in the upper part of the mantle.

At fast- and intermediate-spreading ridges, axial melt lenses are commonly used to separate the cooled, brittle lithosphere above the partially molten crust and mantle below[10], and define the brittle-ductile boundary (BDB). However, at slow- and ultraslow-spreading ridges, in the absence of images of axial melt lenses, the maximum depth of earthquakes, corresponding to the 700 ± 100 °C isotherms[10–12], is used to define the BDB. Based on thermal models, earthquakes are expected to occur at depths <8 km below the seafloor (bsf) beneath slow-spreading ridges and at depths <12 km bsf beneath ultraslow-spreading ridges[13]. However, some deeper earthquakes have recently been observed beneath slow- and ultraslow-spreading ridges[13–15] and have been associated with either deep-rooted detachment faults[14,15] or cold thermal regimes[13,16]. Deep earthquakes have also been observed along oceanic transform faults (TFs), which have been linked to semi-brittle deformation in high-temperature hydrated mylonite shear zones[17,18]. These observations indicate that the maximum depth of earthquakes also depends on other factors, such as tectonic, hydrothermal, and petrological processes.

Here, we present the results of a microseismicity study from the Mid-Atlantic Ridge (MAR) in the equatorial Atlantic Ocean (Fig. 1a). The MAR here spreads at a half-spreading rate of 16 mm/yr[19]. The study area is located in the northern part of the ~200-km-long MAR segment between the Romanche and Chain TFs, in the vicinity of the eastern Romanche ridge-transform intersection (RTI) (Fig. 1a). The studied portion of the ridge is ~120 km in length, offset by two non-transform discontinuities (NTD) (Fig. 1b). It can be subdivided into four 20–50 km-long subsections (Fig. 1b): the RTI segment (named RC1), the first NTD (NTD1), a short ridge segment (named RC2), and the second NTD (NTD2) (Figs. 1–3). The ridge segment south of NTD2 is named RC3. The RTI segment is amagmatic and bounded to the east by a westward dipping detachment fault with a prominent oceanic core complex (OCC) on the eastern side of the ridge axis (Figs. 2a and 3a). The extensive observation of peridotites on the seafloor[20,21] (Figs. 1b

[1]Key Laboratory of Submarine Geosciences, Second Institute of Oceanography, Ministry of Natural Resources, Hangzhou, China. [2]Geo-Ocean UMR6538, CNRS-Ifremer-UBO-UBS, Plouzané, France. [3]Université Paris Cité, Institut de Physique du Globe de Paris, CNRS, Paris, France. [4]Independant scholar, 7 Sondre Skogveien, Bergen, Norway. [5]Cnr-Istituto di Geologia Ambientale e Geoingegneria, Roma, Italy. [6]Department of Chemical and Geological Sciences, University of Modena, Modena, Italy. ✉e-mail: ztyu@sio.org.cn; singh@ipgp.fr

https://doi.org/10.1038/s41467-024-55792-9

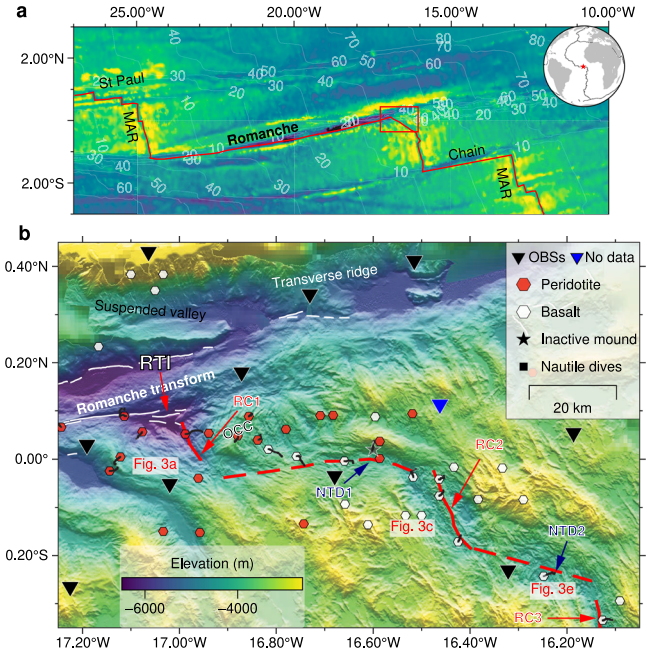

Fig. 1 | Bathymetric map of the study area. a Major transform faults in the equatorial Atlantic Ocean. The inset shows the location on a global map, and the red rectangle marks the study area shown in (**b**). Thin gray lines indicate the lithospheric ages[35] every 10 Ma. MAR: Mid-Atlantic Ridge. **b** Bathymetric map with the location of rock samples in the vicinity of the eastern Romanche-MAR transform-ridge intersection (RTI), showing the area of the seismic experiment carried out during the SMARTIES cruise[21]. Solid and dashed red lines indicate the MAR axes and non-transform discontinuities (NTD) shown in Figs. 2 and 3, respectively, with defined segment names on the side. Rock samples are shown in colored hexagons[20,21] (see legend for symbols). An oceanic core complex (OCC) lies on the outside corner of the MAR. The triangles represent some of the deployed ocean-bottom seismometers (OBSs); the blue triangle indicates the OBS that did not generate seismic data. The black star indicates an inactive hydrothermal mound suggested by the Nautile dive observations (black dive traces)[21]. The white lines show faults along the Romanche transform. The color scale gives the water depth.

and 2a) indicates the presence of the exhumed mantle and supports the tectonic origin of this subsection. The surface of this OCC is heavily cut by roughly N20°E- and N20°W-striking normal faults, suggestive of recent active tectonic deformation (Figs. 2a and 3a). The NTD1 is ~35 km long, oriented at N76°E, and is characterized by a large number of N118°E- and E-W-striking faults (Fig. 3a, c). The presence of both pillow basalts and peridotites on the seafloor (Figs. 1b and 2a)[20,21] indicates its magmatic and tectonic origin. The segment RC2 south of NTD1 is ~22 km long, with a typical 10-km-wide median valley and an N154°E-oriented neo-volcanic ridge (Fig. 3c), suggesting a magmatically robust segment. This is further supported by the extensive observation of basalts on the seafloor (Figs. 1b and 2a)[21]. The NTD2 has an ~33 km ridge offset, oriented at N110°E, with large areas affected by a complex pattern of normal faults, striking at N115°E and N145°E (Fig. 3e). The segment RC3 is a 50 km-long magmatic segment, oriented ~N165°E.

Results

The microseismicity data were acquired by a network of 19 ocean-bottom seismometers (OBSs) during the SMARTIES cruise in 2019[21,22] (Figs. 1–2), covering the 140 km eastern part of the Romanche TF, the RTI, and 120 km of the MAR axis. The seismic data were recorded continuously for ~21 days, with an instrument spacing of ~30 km (Fig. 1b). We detected initial earthquake arrivals automatically from 17 useful OBSs using a short-term-average/long-term-average trigger algorithm[23] (Supplementary Fig. 1). Both P- and S-wave arrivals were then checked manually. An active-source wide-angle seismic refraction profile[24] was used to find the best one-dimensional (1-D) velocity model to calculate travel times during earthquake locations (Supplementary Figs. 2–5). We used a non-linear earthquake location algorithm[25] to obtain earthquake hypocenters, which were then relocated using a double-difference location method[26]. Station corrections (Supplementary Fig. 6) were calculated and updated[25], and S-wave delays due to low-velocity sedimentary layers were removed[18]. Extensive depth resolution tests were carried out to assess the reliability of earthquake locations (Supplementary Figs. 3, 5, 7–9). Local magnitudes of earthquakes were also determined (Supplementary Fig. 10). More details on earthquake locations are presented in the Methods section.

We located 514 earthquakes in the vicinity of the Romanche RTI region (Fig. 2). In this study, we focus on the earthquakes along the ridge segments and discontinuities (RC1, NTD1, RC2, and NTD2). The hypocenters locations along each subsection are shown in Fig. 3. On the basis of well-established criteria[27–29], we have classified our earthquake locations into four categories (A, B, C, and D) (See Methods, Figs. 2 and 3, Supplementary Table 1). Categories A and B are considered of good quality and are used for interpretation.

There are three key observations along these four subsections: (1) a majority of shallow earthquakes (0–6 km) occur on the outside corner of the RTI beneath the OCC faulted dome and off-axis west of the segment RC1; (2) deep microseismicity (~10–20 km) lies beneath the ridge axis of the segment RC2; and (3) normal-depth (4–10 km) earthquakes occur beneath the southern NTD2 (Figs. 2 and 3). Note that this microseismicity record is just a brief snapshot in time, and it provides insight into the processes along this MAR supersegment, even if the microseismic activity may vary substantially over years.

For a full spreading rate of ~32 mm/yr[19], microseismicity studies[13] indicate that the maximum depth of earthquakes should be less than 10 km (Fig. 4, Supplementary Table 2), corresponding to a brittle lithospheric thickness of <10 km. Such a depth range is only observed beneath the OCC (<6 km, Fig. 3b) and NTD2 (<10 km, Fig. 3f). The absence of deep microseismicity beneath the axial valley floor, near the OCC termination (Fig. 3a), suggests that this detachment fault is inactive. However, the shallow earthquakes recorded directly beneath the OCC dome likely result from ruptures on high-angle normal faults cutting its surface. The earthquake distribution and tectonic observations thus suggest that the ridge axis is being relocated from the OCC termination in the axial valley to the east beneath the OCC faulted dome[20]. Beneath the NTD2, the earthquakes are slightly deeper, down to ~10 km (Fig. 3e, f), which is expected for a slow-slipping NTD (Fig. 4, Supplementary Table 2). These results suggest that the brittle lithosphere is at most ~10 km thick at the segment boundaries (NTDs).

The BDB is expected to become shallower southward with increasing distance to the RTI because of the decrease in the cold-edge effect caused by the cold (45 Ma) lithosphere[20,30,31]. However, we observed deep earthquakes (16–19 km) beneath the segment RC2 axis (Fig. 3c, d). These are the deepest earthquakes documented to date at a slow-spreading center (Fig. 4). Seismic refraction studies indicate that the 8-Ma-old crust of the western ridge flank is 5.4 ± 0.3 km thick[32], suggesting that these earthquakes mostly occur in the mantle below 10 km depth, with some scattered events in the crust (Fig. 3d), far exceeding the suggested maximum depth range (Fig. 4). An earthquake cluster is also observed on the western side of the axial valley, with shallow focal depths (~2–6 km) (Fig. 3d), suggesting that the unexpected depths of the events beneath the MAR axis are not an artifact of location errors. The depth resolution tests (Methods, Supplementary Figs. 7–9) further support that these events are indeed deep.

Discussion

The maximum depth of earthquakes beneath this portion of the MAR does not follow the relationship between BDB depth and spreading

https://doi.org/10.1038/s41467-024-55792-9

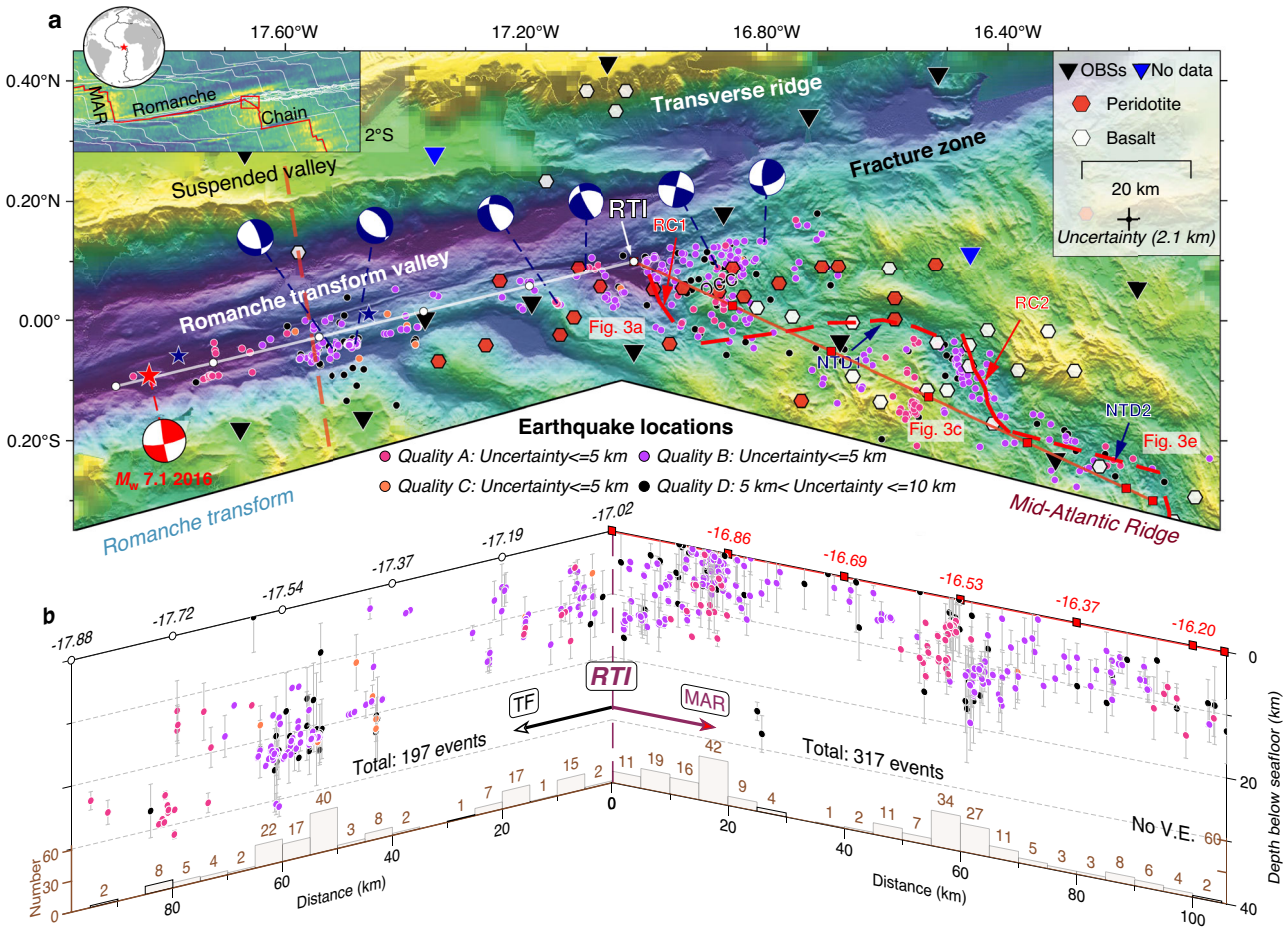

Fig. 2 | Map of the microseismicity and earthquake depth along the Mid-Atlantic ridge study region. a Bathymetric map with microseismicity in the study region, whose location is shown in the inset map on the upper left corner, in which white lines indicate the lithospheric ages[35] every 10 Ma. The colored circles indicate determined earthquakes in this study with different location qualities (Methods, Supplementary Table 1). The average horizontal uncertainty (~2.1 km) after earthquake relocation is marked by a black plus sign (see legend for symbols). Focal mechanisms (Supplementary Table 5) are shown in blue and white beach balls. The red star with a beach ball and the two blue stars indicate the 2016 M_w 7.1 Romanche earthquake and two subevents, respectively[78]. The dashed red line shows the seismic refraction profile[24]. The other labeling is the same as that in Fig. 1b. **b** Earthquake depths along the Romanche TF (white line in **a**) and along the MAR (red line in **a**) within ±10 km of the profile. The bottom histograms show the number of earthquakes along the profile. The zero position is the RTI location. The white circle and red squares on the top mark the 20 km intervals and longitudes for reference. Depth uncertainties are plotted in gray lines.

rate[13] observed elsewhere (Fig. 4). One explanation for these deep earthquakes is that they are due to an extremely cold and thick lithosphere[13,16], where the BDB would be ~20 km deep, corresponding to the 600–800 °C isotherms[10–12], similar to what was proposed for the Southwest Indian Ridge (SWIR)[33]. However, the presence of a hummocky volcanic axial morphology, volcanic cones, and a well-defined neo-volcanic ridge in the axial valley (Fig. 3c) indicates that the segment RC2 is of magmatic origin, unlike the smooth morphology related to amagmatic spreading processes at the SWIR[34], where the lithosphere is cold and thick. The axial valley floor here is characterized by bathymetric highs, cut by ridge-parallel normal faults (Fig. 3c) and shows basaltic constructions confirmed by basaltic rocks observed on the seafloor (Fig. 1b). In addition, the off-axis shallow microseismicity (down to 6 km) west of the segment RC2 axis (cross-section dd′, Fig. 3c, d) indicates that the BDB remains shallow (<10 km depth) up to a crustal age of ~1.3 Ma[35] in the vicinity of the MAR (Fig. 3c). Moreover, the microseismicity down to 10 km beneath NTD2 reveals that the BDB is indeed at ~10 km (Fig. 3f), which is normal for a slow-spreading ridge and NTD (Fig. 4), but it is much shallower than the deep microseismicity observed beneath the segment RC2. Thermal modeling[31] suggests that the temperature should be 1100–1200 °C at 10–20 km depth, and hence the mantle beneath this RC2 segment axis is hot, as expected for a typical magmatic segment.

One hypothesis to explain the large earthquake depths is that a robust hydrothermal circulation cools the lithosphere rapidly away from the ridge axis[36], therefore, the temperature-controlled seismicity and the BDB[13,16] would deepen due to the cooling effect of hydrothermal circulation. To date, there are no observations of active hydrothermal vents on the segment RC2 axis. However, an extinct hydrothermal vent field is observed on the eastern flank of the NTD1[21] but its location is relatively far from the present-day axial valley (Fig. 3c), and hence would not affect the lithosphere beneath the segment RC2 axis. Taken together, these results indicate that magmatism dominates the crustal accretion process at the segment RC2, and these earthquakes occur in a hot mantle at temperatures >1100 °C.

Another hypothesis for the presence of deep earthquakes is the development of a localized high strain[37] in semi-brittle high-temperature mylonite shear zones in the mantle along TFs[17,18]. A localized high-strain shear zone in the deep mantle beneath spreading centers can be expected to occur during the development of detachment faults[14,15,38], producing deep microseismicity. However, this hypothesis is not supported by the observations, as the 10-km-wide axial valley at the

https://doi.org/10.1038/s41467-024-55792-9

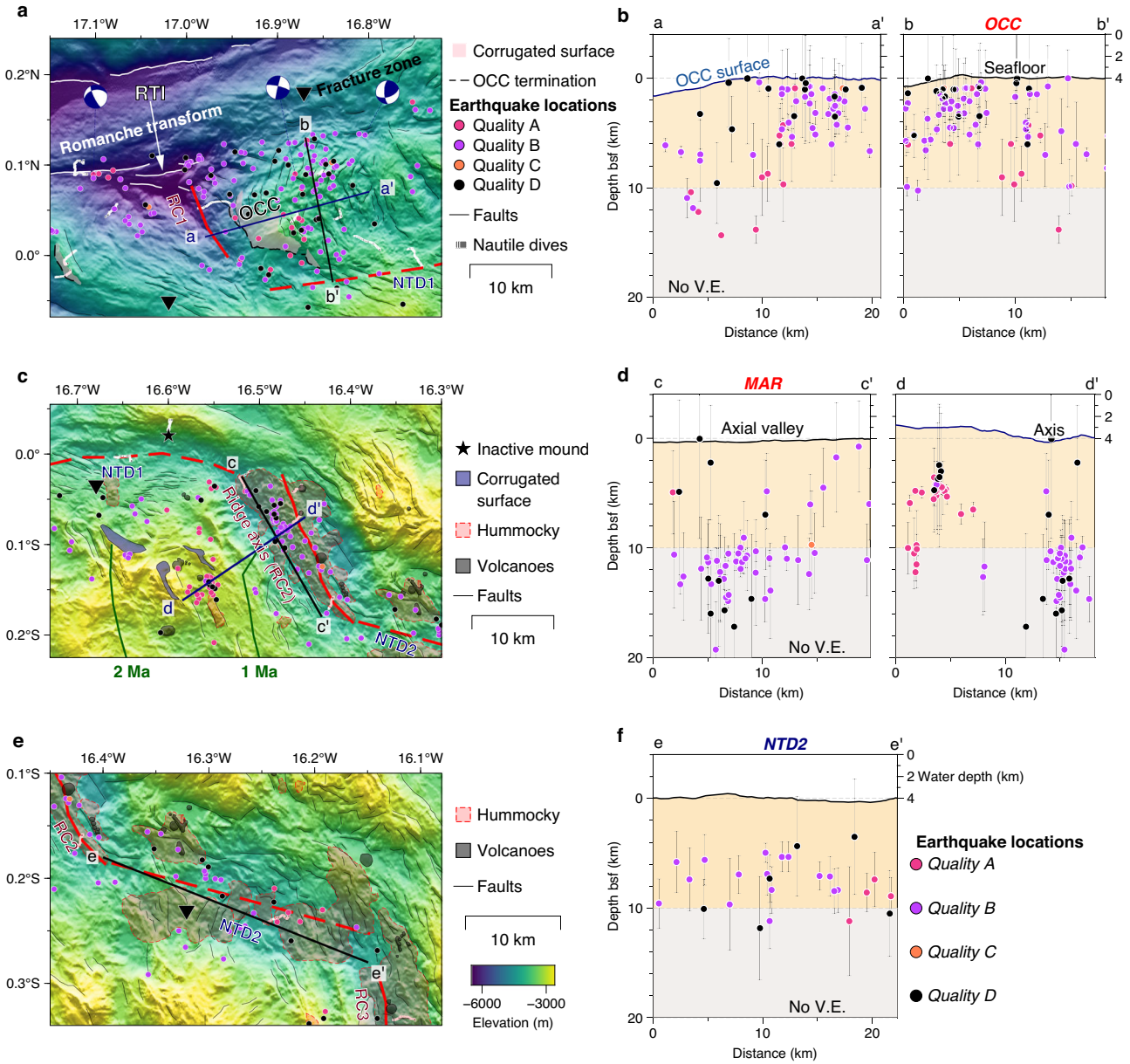

Fig. 3 | Microseismicity and tectonics at different segments. a Bathymetric map of the RTI area showing earthquakes and focal mechanisms. Tectonic information, including the corrugated surface of the OCC (pink shade), faults (black lines), transform fault trace (white lines), and termination of the OCC (dashed lines), is marked (see legend for symbols). Earthquakes with different location qualities (Method, Supplementary Table 1) are shown in colored circles. Blue and white beach balls indicate determined focal mechanisms. **b** Two transects of earthquake depth profiles, within ±5 km of the profile, along and across the OCC are marked by aa′ and bb′ in (**a**), respectively. The seafloor depth is marked on the upper part. Light brown areas indicate earthquake depths of <10 km and gray for event depths of >10 km. **c** Bathymetric map, events, and geological information along the segment RC2. Hummocky seafloor and volcanic cones are shown in red and gray shades, respectively. The corrugated surfaces are marked in blue shades. The dark green lines indicate the lithospheric ages[35]. **d** Two transects of earthquake depths along (cc′) and across (dd′) the ridge axis. **e** Bathymetry, earthquakes, and geological information along the southern NTD (NTD2). **f** A transect of earthquake depth along the NTD2 (ee′). The other labels are the same as those in Fig. 1b.

segment RC2 is bounded by high-angle NNW-SSE oriented inward dipping faults (Fig. 3c) and does not show any evidence for the presence of detachment faults.

The third possibility is that these deep earthquakes in the mantle are associated with magmatic-tectonic activities, similar to those observed in Askja Volcano[39–42] and Fagradalsfjall Peninsula[43,44] in Iceland (depths >10 km) and offshore Mayotte Island in the western Indian Ocean (depths >30 km)[45]. Melt movement at depth introduces high strain rates, producing brittle failure in the ductile lower crust[39,41]. Furthermore, pre-existing faults and fractures above a deep magma reservoir can favor melt migration[45], producing earthquakes. However, such magmatic-tectonic events (Asjia[39–42], Mayotte[45], Fagradalsfjall[43,44]) are associated with volcanic eruptions, where the strain induced by magma and/or CO_2-fluid movement[44] is much stronger than that beneath a normal ridge segment. Also, the seismicity in Iceland occurs in a thickened crust[39,41], and in the case of Mayotte, it occurs in a cold lithosphere[45]; both contexts are different from a mid-ocean ridge. In our case, there is no evidence of a current volcanic eruption in the axial valley, as indicated by the low level of crustal microseismicity and the seafloor morphology (Fig. 3c). The deep earthquakes beneath the segment RC2 axis are aligned along a ~N150°E direction, thus paralleling the main axial normal faults (Fig. 3c), and not in a cluster or

https://doi.org/10.1038/s41467-024-55792-9

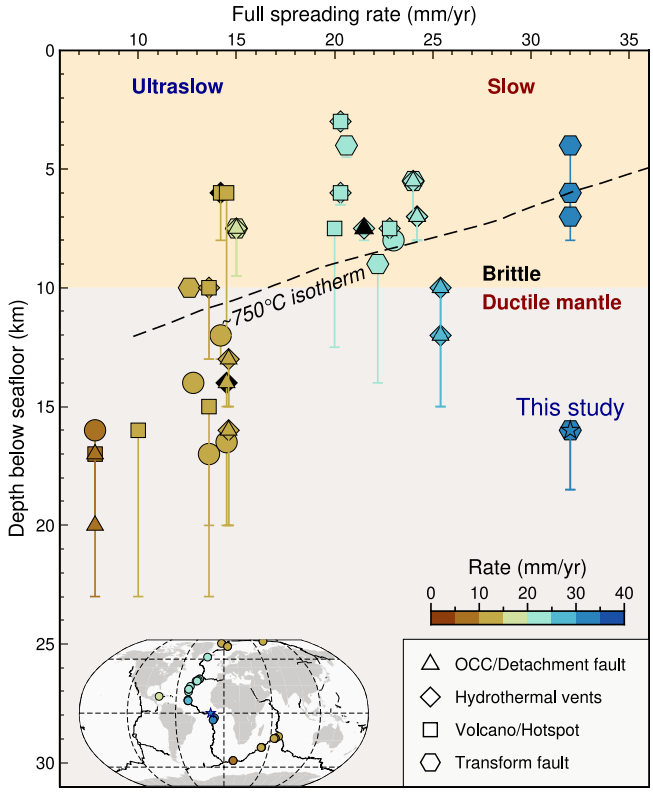

Fig. 4 | Statistics for the maximum depth distribution of microseismicity and full spreading rates. The depths of earthquakes for slow- and ultraslow-spreading ridges are shown in blue and brown circles, respectively, whose locations are shown on the inset map. The color scale gives full spreading rates. The dashed black line indicates the 750 °C isotherm[10]. The maximum depths are affected by several processes, e.g., detachment faults (triangles), hydrothermal vents (diamonds; a black one is inactive), volcanoes or hotspots (squares), and TFs (hexagons) (see legend for symbols). A compilation of all the depth data and references used in this figure is given in Supplementary Table 2.

swarm (Supplementary Fig. 11) as those reported for magmatic-tectonic events[41,44,45]. Therefore, we suggest that the mechanism of melt movement does not apply to these earthquakes. On the contrary, the swarm-like off-axis shallow microseismicity (<10 km) west of the ridge axis (Fig. 3c, d) is probably related to off-axis magmatism in the crust.

The fourth possibility, and our preferred, is that the observed deep microseismicity beneath the segment RC2 is related to CO_2 degassing from the ascending melt. In magmatic systems, the volatile element concentration controls the evolution of the physical properties of the magma and plays a key role in the dynamic of eruptions. The degassing causes a volume change, which in the presence of extensional stresses[46,47] produces locally high strain rates and triggers deep earthquakes in the mantle. As the solubility of CO_2 in silicate melts is strongly dependent on pressure (and H_2O concentration)[48], the degassed CO_2 would be dissolved in the liquid phase at depth (high pressure) but would saturate and nucleate a gas phase (80–90% loss)[48] by the time it reaches the seafloor. Given that an increase in pore pressure of only 2–3 bars can trigger earthquakes[49], we suggest that the small pressure increase due to CO_2 degassing from the ascending melt induces the earthquakes observed beneath the RC2 ridge axis[46,47].

We compiled all published geochemical analyses of MORB samples collected within the bounds of our OBS network coverage (Methods, Fig. 5). In order to investigate their pre-eruptive CO_2 concentration, previous studies have examined volatile/non-volatile element ratios[50–53]. At depth, during partial melting and fractional crystallization, the geochemical behavior of CO_2 is similar to that of highly incompatible trace elements[50–53]. Rare undegassed mid-ocean ridge basalts (MORBs) and olivine melt inclusions have allowed to define global trends in the ratios of volatile to non-volatile incompatible trace elements, such as CO_2/Rb (991 ± 129)[51], and CO_2/Ba (81.3 ± 23)[51] (Methods, Fig. 5). These correlations have been used to calculate the primary melt CO_2 content of global ridge segments[51]. It should be noted that estimating CO_2 concentrations from trace element abundances relies on the assumption that the trace elements are reflective of the mantle source and have not been affected by secondary processes. In the segment RC2, all samples are enriched in incompatible trace elements (Rb >8 ppm, and Ba >89 ppm) compared to the samples from the southern segment RC3, or normal MORBs[54–56] (Fig. 5, Supplementary Data 1). After correcting for fractional crystallization, we calculated CO_2 concentrations in melts in equilibrium with their mantle source using both Rb_{90} and Ba_{90}[51,57] (see Methods). Melts generated along the segment RC2, where deep mantle earthquakes are observed, also appear significantly enriched in volatiles ($CO_{2(calculated)}$ = 0.4–3.0 wt%) (Fig. 5, Supplementary Data 1), compared to the segment RC3 ($CO_{2(calculated)}$ = 0.04–0.7 wt%) (Fig. 5, Supplementary Data 1). These highly enriched basalts and high volatile contents have been reported by previous geochemical studies and have been interpreted as the result of low degrees of partial melting of an enriched mantle source near the Romanche TF[54–56].

On their way to the surface, these melts seem to have undergone fractional crystallization, leading to estimated pre-eruptive CO_2 concentrations ranging from 0.7 wt% to 4.6 wt% for the segment RC2 (See Methods, Supplementary Data 1). Existing CO_2 measurements[54–56] in the samples along the segments RC2 and RC3 have concentrations very close to the CO_2 solubility calculated based on the hydrostatic pressure at the sample depth (Methods, Supplementary Data 1). This is to be expected as seafloor basalts are mostly degassed. Using the CO_2 solubility model[58], the melt (>0.7 wt% CO_2) would become saturated with CO_2 at ~0.7 GPa (~25 km depth) and 1250 °C and would start degassing CO_2, in agreement with the observed deep microseismicity. However, no earthquakes are observed at depths >20 km beneath the RC2 ridge axis (Fig. 3d), which could be due to higher temperatures (>1200 °C) at >20 km depths[31] (Fig. 6) that would hinder the nucleation of earthquakes.

The seismic nucleation mechanism proposed here is similar to that generated by fast magma expansion and associated pressure variations due to the rapid degassing of CO_2 beneath active volcanoes[59,60]. This mechanism may result in deep long-period volcanic earthquakes[61]. The spectral analyses of seismic data indeed show some deep earthquakes without high-frequency energy (>5 Hz) (Supplementary Fig. 12), implying that these earthquakes may be long-period events[60]. However, not all events are characterized by low-frequency energy, and more earthquakes would be required to study the characteristics of their sources in the future.

Based on our model (Fig. 6), at ultraslow-spreading ridges (e.g., SWIR and Gakkel Ridge) where deep mantle earthquakes have been observed[13,62], the CO_2 content is likely to be high. Previously, the highest amount of CO_2 in the melt has been reported at the SWIR (1.9 wt%)[51]. Between 5°S and 5°N in the equatorial Atlantic Ocean, previous studies[32,51,52] have suggested that the CO_2 concentrations at several segments are generally high, reaching an average of ~2800 ppm and up to ~8799 ppm based on the CO_2/Rb and CO_2/Ba estimations[51] (Supplementary Fig. 13). As the melt migrates towards the surface, it would continue to degas, producing earthquakes in the mantle between 10 km and 20 km.

Keller et al.[63] suggested that the presence of volatiles in the ascending melt does not only focalize melt beneath the ridge axis but also flushes melt away from the axial area that may accumulate at the lithosphere-asthenosphere boundary (LAB). Recent studies from the equatorial Atlantic region[64,65] show that volatiles would reduce the

https://doi.org/10.1038/s41467-024-55792-9

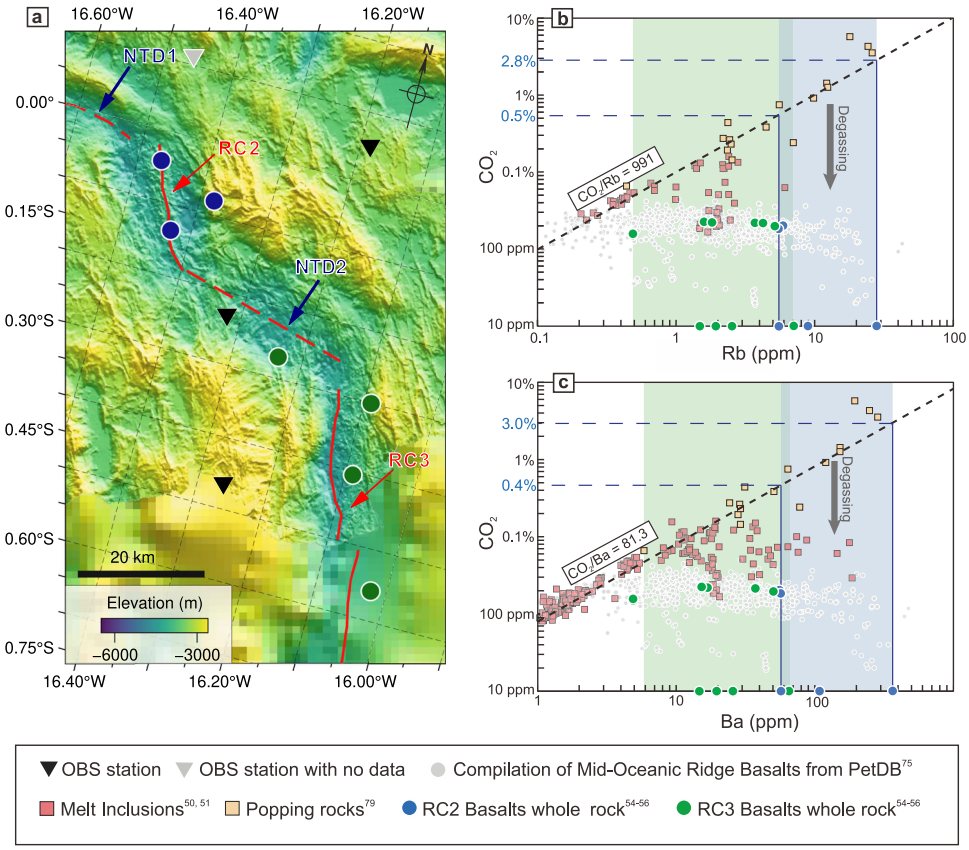

Fig. 5 | CO_2 contents as a function of element composition. a Locations of the rock samples in the vicinity of the present MAR segment. Blue and green dots indicate the MORB samples along the segments RC2 and RC3, respectively. The CO_2 content as a function of Rb (**b**) and Ba (**c**) for MORB whole rocks (gray circles) from the PetDb database[75], popping rocks (yellow squares)[79], and melt inclusions (red squares)[50,51] (see legend for symbols). The measured CO_2 contents[54–56] of the rock samples along the segments RC2 and RC3 are also presented. The dashed blue lines and numbers indicate the estimated CO_2 contents in the primary melt on each map.

solidus temperature of the anhydrous peridotite, resulting in the presence of melt at sub-solidus temperatures for anhydrous peridotites (~1250° C) at the LAB. To explain the reflections at the LAB, Audhkhasi and Singh[64] proposed that ~1.1 % of melt is required at the base of the LAB, with a water content of up to 332 ppm. A large amount of CO_2 in the melt, according to our analysis and previous studies[51,56] suggests that the presence of melt at the LAB could be due to a combination of CO_2 and H_2O[63]. The presence of a large amount of volatiles would also extend the depth of incipient volatile-bearing melting beneath spreading centers[2,4]. The observation of microseismicity at 10–20 km depth suggests that ascending melt resides in the mantle at these depths, fractionates, and evolves[6], before moving upwards to form the oceanic crust. The melt could also freeze at the base of the lithosphere, producing sub-horizontal reflections as observed beneath the young Juan de Fuca plate[36] and leading to high compositional heterogeneities in the oceanic lithosphere[36,63].

Methods

Seismic data

In July and August 2019, we conducted an OBS passive seismic experiment (Figs. 1–3) during the SMARTIES cruise[21,22]. A network of 19 OBSs was deployed, with an instrument spacing of ~30 km (Fig. 2a). We first detected earthquake arrivals automatically using a short-term-average/long-term-average trigger algorithm within the SEISAN package[23] by analyzing the vertical components of 17 useful OBSs (Supplementary Fig. 1). In total, 760 earthquakes were identified and registered into the SEISAN database. Each of these events was then checked manually to make sure they were detected by at least five OBSs.

The reference one-dimensional (1-D) velocity model

The velocity structure of the study region is important for the precision of earthquake locations, and the closer it is to reality, the better earthquake locations will be. We constructed five 1-D P-wave velocity models (Supplementary Fig. 2a), derived from an active-source wide-angle seismic refraction profile[44], which provides velocity constraints at depths down to ~60 km below sea level. They include models beneath the northern flank, the transform valley, and the southern flank of the Romanche TF, a low-velocity model beneath the transform valley, and an average velocity model from north to south across the Romanche TF (Supplementary Fig. 2a). Then we used the five 1-D velocity models to locate earthquakes and selected the one exhibiting the best possible combination of a large number of located events and a low average root mean square (RMS) residual (Supplementary Fig. 2b, Supplementary Table 3). We found that the average velocity model (Model 5 in Supplementary Fig. 2a) was the best-fitting model (Supplementary Fig. 2b, Supplementary Table 3), and hence was selected for the subsequent earthquake location and focal mechanism computation.

To further evaluate the choice of the selected velocity model, we constructed a 360-earthquakes sub-dataset, each with ≥6 arrivals and station GAP ≤ 180°, and used the VELEST program[66] to search for the ″minimum 1-D velocity model″ to locate earthquakes (Supplementary Fig. 3). The results indicate that after six iterations, the RMS residuals of the two models are close, but our selected velocity model leads to more located earthquakes than the ″minimum″ velocity model (Supplementary Fig. 3). Thus, we prefer to use the selected velocity model (Model 5 in Supplementary Fig. 2a) for the next earthquake location. Finally, 514 earthquakes were located (Fig. 2), with depth uncertainties

https://doi.org/10.1038/s41467-024-55792-9

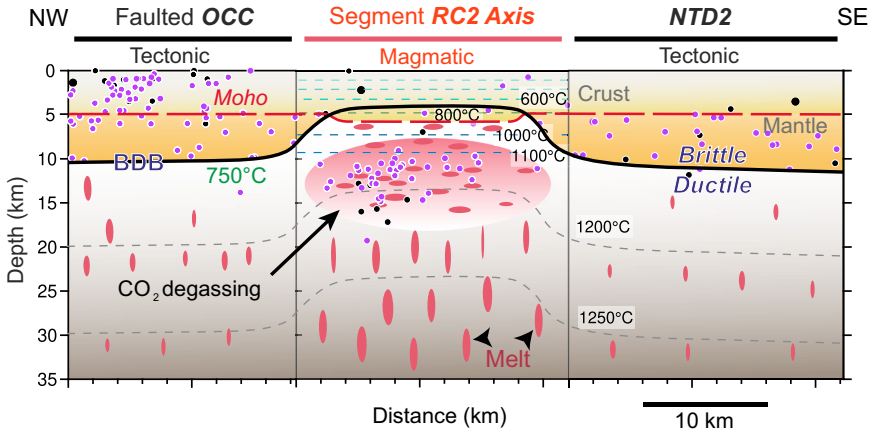

Fig. 6 | Schematic diagram showing the microseismicity along the MAR axis. Three segments are illustrated southward from the Romanche TF. The brown and gray patches indicate the brittle and ductile lithospheres, respectively. The thick black line represents the BDB constrained by the maximum depth of earthquakes, corresponding to the 750 °C isotherm[10]. The crust beneath the segment RC2 is ~5.4 ± 0.3 km thick[32], and the expected Moho interface is shown in a dashed red line. Deep earthquakes (10–19 km bsf) beneath the MAR axis are interpreted as a result of volume change due to CO_2 degassing from the ascending melts in the hot ductile mantle. Colored dashed lines indicate the temperature isotherms extracted from a simulated thermal model[31].

of ≤10 km, horizontal uncertainties of ≤10 km, RMS residuals of ≤0.3 s, and station gaps of <270°. Their mean horizontal and vertical errors are ~2.8 km and ~2.9 km, respectively (Supplementary Table 3).

Wadati diagrams yield a Vp/Vs ratio of ~1.7 (Supplementary Fig. 4), which is used to estimate the S-wave velocity in inversion. To further examine the choice of the Vp/Vs ratio, we used various Vp/Vs ratios ranging from 1.5 to 2.5 to locate earthquakes (Supplementary Fig. 5). The results show that the Vp/Vs ratio of ~1.7 has the lowest RMS residuals and the largest number of located earthquakes among all tests (Supplementary Fig. 5), indicating that the Vp/Vs ratio setting of ~1.7 is reasonable. The seismic tomographic results[67] also indicate normal Vp/Vs ratios in the present segment RC2.

Earthquake location

We used the non-linear oct-tree search algorithm of the NonLinLoc program[25] to locate initial earthquake hypocenters, of which the maximum likelihood solution was selected as the preferred result. NonLinLoc estimates a 3-D error ellipsoid (68% confidence) from the posterior density function scatter samples[25]. Iterative calculations of station corrections (Supplementary Fig. 6) were used to find the best solution as well as to remove the 3-D effects when the average RMS misfit yields a minimum (Supplementary Fig. 2b). At the same time, we removed the S-wave delays, which may be caused by very low velocities associated with unconsolidated sediments[13], from the original S-onsets before inversion[18].

After removing the S-wave delays, double-difference relocations for 364 well-constrained events were determined using the hypoDD program[26]. All 364 earthquakes were detected on more than six OBSs, with RMS residuals of <0.25 s, uncertainties of <5 km, and azimuthal gaps of <270°. We performed the relocation using differential travel times from the original catalog and waveform cross-correlation data. Station corrections (Supplementary Fig. 6) obtained by the NonLinLoc program were successfully applied. A minimum of six catalog links per event pair was required to form a continuous cluster. Five iterations were carried out, with a maximum event separation of 6 km. As a result, 276 events were well relocated, and they replaced the NonLinLoc locations in the final catalog. As a result, 317 events were located along the MAR and 197 events along the Romanche TF (Fig. 2b), with an updated average horizontal uncertainty of ~2.1 km (Fig. 2a).

We followed well-established criteria[27–29,68] to assess the reliability of our earthquake locations. For a well-constrained earthquake location, the following criteria can be used[27]: (1) the azimuthal station gap is <180°[68]; (2) there are more than eight arrivals to locate an earthquake, with at least one S-wave arrival and one arrival within a focal depth distance from the epicenter[29]; (3) one S-wave arrival is recorded within 1.4 times of the focal depth distance from the epicenter[28]. Based on these criteria, we classified our earthquakes into four categories (Supplementary Table 1). The earthquakes with location category A meet all the above criteria, and those with location quality B-C meet two criteria, whereas the events with location quality D only meet one criterion. We find that ~78% of the located earthquakes meet at least two criteria (see details in Supplementary Table 1), and hence we can confidently interpret these hypocenter locations.

Depth resolution

To gain insight into the effect of uncertainty in velocity on the earthquake location, earthquake depths were determined using five different velocity models (Supplementary Fig. 2a, Supplementary Fig. 7). We find that the depths of most of the axial events remain between 10 and 20 km, and the depth shifts are smaller than the average depth uncertainties (~2.6 km) (Supplementary Table 3). However, the fastest model (Model 1), which is derived from the southern Romanche TF[24], leads to some shallow events in the crust beneath the axial valley (Supplementary Fig. 7d). Notice that this model shows that the P-wave velocity exceeds 7.2 km/s at ~3 km depth, which is unusual for a magmatically accreted young crust (<7.5 Ma[69]) (Supplementary Fig. 7b). Although the southernmost flank of the Romanche TF is believed to be composed of mantle peridotites, representing a crust-free lithosphere (Fig. 1b)[18,21,30], this model is not appropriate for locating events beneath the MAR axis. To investigate the effect of velocity uncertainty further, we increased and decreased the velocity by ±0.1 km/s at all depths (Supplementary Fig. 8, Supplementary Table 4). We find that both the lower and higher velocities result in locating a substantial number of deep events (>10 km) beneath the ridge axis (Supplementary Fig. 8c–e). Although the increased velocity model leads to some shallow events, it is also accompanied by a decrease in the number of located earthquakes (Supplementary Table 4). Interestingly, the reduced velocity model leads to a smaller depth uncertainty (Supplementary Fig. 8c–e), and therefore, it is reasonable to use a normal or slightly decreased velocity model in the study area rather than an increased velocity model. To further validate the robustness of the deep earthquake locations beneath the segment RC2, we constructed a subset of 45 events at depths ranging from 10 to 20 km along the cross-section cc′ shown in Fig. 3d. Their depths were then forced to be unchanged at 2.5 km, 5 km, 7.5 km, and 10 km during the relocation process. We find that not only their initial RMS residuals were much

higher but they decreased much more slowly, and the final RMS were higher than those obtained when the depths were not fixed. (Supplementary Fig. 9). All these tests indicate that the deep events beneath the ridge axis (RC2) are well constrained, required by the data, and not artifacts (Supplementary Figs. 7–9).

Magnitude estimation

Earthquake magnitudes were determined using the local magnitude scale M_L[70]:

$$M_L = logA + 1.11log(D) + 0.00189D - 2.09$$

The maximum amplitude A is measured on a seismogram simulating the original Wood-Anderson seismogram using the SEISAN package[23]. D is the hypocentral distance in kilometers. The magnitude completeness (M_C, 1.5) and b value (0.87) are also calculated using the ZMAP software[71] (Supplementary Fig. 10a). Earthquakes were divided into three groups, i.e., events along the TF, in the ridge-transform intersection, and along the MAR (Supplementary Fig. 10b–d). Their b values were also determined, with small differences from each other (0.89–0.93) (Supplementary Fig. 10).

Focal mechanism solution

We used the P-phase first-motion polarities to determine focal mechanisms using the HASH package[72], and these polarities were picked from unfiltered earthquake waveform data on the vertical component. As previously noted[18], the resulting mechanism solutions are not very robust, mainly due to the large spacing of OBSs (~30 km) (Fig. 2a). Also, the poor azimuthal ray path distribution limits the quality of the results. Using a selection criterion based on P-wave polarities of >8, an azimuthal gap of <180°, an RMS fault plane uncertainty of <45°, average misfit <20%, station distribution ratio of >0.4, and mechanism probability >60% (Supplementary Table 5), we obtained three new well-constrained focal mechanism solutions (Fig. 2a), which combined with the three previous solutions for earthquake swarms[18], provided six focal mechanisms (Supplementary Table 5).

The maximum depth of earthquakes

We compiled the maximum depth of earthquakes along the ridge axis documented to date at slow- and ultraslow-spreading ridges around the world, as well as the full spreading rate on each site[19] (Fig. 4, Supplementary Table 2). In this study, we selected the maximum depths that were well constrained by several earthquakes instead of only one event to avoid bias in the location process (Supplementary Table 2). In addition, we included information that may influence the maximum depth distribution, such as the presence of oceanic core complexes and/or detachment faults, hydrothermal vents, magmatism (e.g., focused melting and/or hotspots), and adjacent TFs (Fig. 4, Supplementary Table 2). It should be noted that the reported data from the SWIR segment 8, SWIR oblique Supersegment, and the Logachev Seamount of Knipovich Ridge were updated using the newly located data[13,73,74]. The Rainbow massif is located at a non-transform discontinuity (Supplementary Table 2), which is also included in the plot for reference (Fig. 4).

CO_2 estimation from MORB

We compiled the MORB samples along all the spreading ridge segments from the PetDB database[75] (www.earthchem.org/petdb) within the bounds of our OBS network (Fig. 5, Supplementary Data 1). In particular, we analyzed the samples in the studied segment RC2 and the adjacent segment RC3 in the south (Fig. 5, Supplementary Data 1). The CO_2/Rb or CO_2/Ba ratios of melt inclusion from the MORBs are a good proxy for the CO_2 concentration[50–53]. Using a constant CO_2/Rb ratio (991 ± 129)[51] (Fig. 5b) and CO_2/Ba ratio (81.3 ± 23)[51] (Fig. 5c), we estimated CO_2 content in pre-eruptive melts for the segments RC2 and RC3. $CO_{2(Rb)}$ and $CO_{2(Ba)}$ are the CO_2 concentrations estimated from Rb and Ba, respectively. For the segment RC2, we find $CO_{2(Rb)}$ = 0.9–4.3 wt% and $CO_{2(Ba)}$ = 0.7–4.6 wt% (Supplementary Data 1). For the segment RC3, our estimated CO_2 values are significantly lower, $CO_{2(Rb)}$ = 0.07–1.0 wt% and $CO_{2(Ba)}$ = 0.06–0.8 wt% (Supplementary Data 1). Primary melts are in equilibrium with their mantle source and are, therefore, different from the pre-eruptive melts, which go through various degrees of fractional crystallization. We calculated Ba_{90} and Rb_{90} as the concentrations of those elements in melts in equilibrium with Fo_{90} olivine[51,57] and used these values to get an estimated CO_2 content in primary melts (Fig. 5, Supplementary Data 1). We find that the CO_2 content in the primary melts is estimated as CO_2 (Rb_{90}) = 0.5–2.8 wt% and CO_2 (Ba_{90}) = 0.4–3.0 wt% for the segment RC2, and CO_2 (Rb_{90}) = 0.05–0.7 wt% and CO_2 (Ba_{90}) = 0.04–0.5 wt% for the segment RC3 (Fig. 5, Supplementary Data 1). These results suggest that the CO_2 concentration in the primary melts is at least 0.4 wt% along the studied segment RC2. In addition, to investigate whether the seafloor basalts are mostly degassed, we calculated CO_2 theoretical solubility for samples with existing CO_2 measurement, based on the model of Iacono-Marziano et al.[76], with the following parameters: dredge depth, a temperature of 1200 °C, and major elements concentration. The calculation results show that the CO_2 solubility values are very close to the measured CO_2 contents (Supplementary Data 1), indicating that those samples are degassed.

Data availability

The raw seismic data and cruise reports are available on the website (https://campagnes.flotteoceanographique.fr/campagnes/18001107/) and can be requested for scientific purposes. The earthquake catalog and picked P- and S-arrivals generated in this study have been deposited in the Zenodo database (https://doi.org/10.5281/zenodo.12696684).

Code availability

The SEISAN software[23] used to pick phases is available at https://www.geo.uib.no/seismo/SOFTWARE/SEISAN/. The NonLinLoc code[25] used for earthquake location is available at http://alomax.free.fr/nlloc/. The VELEST program[66] used for inverting the 1-D velocity model is available at https://seg.ethz.ch/software/velest.html. The HypoDD program (version 1.3)[26] used for double-difference earthquake relocation is available at https://www.ldeo.columbia.edu/~felixw/hypoDD.html. The ZMAP software[71] used for catalog analysis to obtain b-value and magnitude completeness is available at https://github.com/swiss-seismological-service/zmap7. The HASH software[72] (version 1.2) used for determining focal mechanisms solution is available at https://www.usgs.gov/node/279393. The Global Mapper used for structural analysis is available at https://www.bluemarblegeo.com/global-mapper/. The GMT 6 toolbox[77] used for graphing is available at https://www.generic-mapping-tools.org/download/.

References

1. McKenzie, D. The extraction of magma from the crust and mantle. *Earth Planet. Sci. Lett.* **74**, 81–91 (1985).
2. Dasgupta, R. et al. Carbon-dioxide-rich silicate melt in the Earth's upper mantle. *Nature* **493**, 211–215 (2013).
3. Dasgupta, R. & Hirschmann, M. M. Melting in the Earth's deep upper mantle caused by carbon dioxide. *Nature* **440**, 659–662 (2006).
4. Dasgupta, R., Hirschmann, M. M. & Smith, N. D. Water follows carbon: CO2 incites deep silicate melting and dehydration beneath mid-ocean ridges. *Geology* **35**, 135 (2007).
5. Ahern, J. L. & Turcotte, D. L. Magma migration beneath an ocean ridge. *Earth Planet. Sci. Lett.* **45**, 115–122 (1979).

6. Klein, E. M. & Langmuir, C. H. Global correlations of ocean ridge basalt chemistry with axial depth and crustal thickness. *J. Geophys. Res.* **92**, 8089 (1987).
7. Langmuir, C. H., Klein, E. M. & Plank, T. Petrological systematics of mid-ocean ridge basalts: constraints on melt generation beneath ocean ridges. In: *Geophysical Monograph Series* (eds. Morgan, J. P., Blackman, D. K. & Sinton, J. M.) 183–280 https://doi.org/10.1029/GM071p0183 (American Geophysical Union, Washington, D. C., 1992).
8. McKenzie, D. The generation and compaction of partially molten rock. *J. Petrol.* **25**, 713–765 (1984).
9. McKenzie, D. & Bickle, M. J. The volume and composition of melt generated by extension of the lithosphere. *J. Petrol.* **29**, 625–679 (1988).
10. Phipps Morgan, J. & Chen, Y. J. Dependence of ridge-axis morphology on magma supply and spreading rate. *Nature* **364**, 706–708 (1993).
11. Chen, W.-P. & Molnar, P. Focal depths of intracontinental and intraplate earthquakes and their implications for the thermal and mechanical properties of the lithosphere. *J. Geophys. Res. Solid Earth* **88**, 4183–4214 (1983).
12. Mckenzie, D., Jackson, J. & Priestley, K. Thermal structure of oceanic and continental lithosphere. *Earth Planet. Sci. Lett.* **233**, 337–349 (2005).
13. Grevemeyer, I. et al. Constraining the maximum depth of brittle deformation at slow- and ultraslow-spreading ridges using microseismicity. *Geology* **47**, 1069–1073 (2019).
14. deMartin, B. J., Sohn, R. A., Pablo Canales, J. & Humphris, S. E. Kinematics and geometry of active detachment faulting beneath the Trans-Atlantic Geotraverse (TAG) hydrothermal field on the Mid-Atlantic Ridge. *Geology* **35**, 711–714 (2007).
15. Parnell-Turner, R. et al. Oceanic detachment faults generate compression in extension. *Geology* **45**, 923–926 (2017).
16. Searle, R. C. & Escartín, J. The Rheology and Morphology of Oceanic Lithosphere and Mid-Ocean Ridges. in *Geophysical Monograph Series* (eds. German, C. R., Lin, J. & Parson, L. M.) 63–93 https://doi.org/10.1029/148GM03 (American Geophysical Union, Washington, D. C., 2013).
17. Kohli, A., Wolfson-Schwehr, M., Prigent, C. & Warren, J. M. Oceanic transform fault seismicity and slip mode influenced by seawater infiltration. *Nat. Geosci.* **14**, 606–611 (2021).
18. Yu, Z. et al. Semibrittle seismic deformation in high-temperature mantle mylonite shear zone along the Romanche transform fault. *Sci. Adv.* **7**, eabf3388 (2021).
19. DeMets, C., Gordon, R. G. & Argus, D. F. Geologically current plate motions. *Geophys. J. Int.* **181**, 1–80 (2010).
20. Bonatti, E. et al. Diffuse impact of the Mid-Atlantic Ridge with the Romanche transform: an ultracold ridge-transform intersection. *J. Geophys. Res. Solid Earth* **101**, 8043–8054 (1996).
21. Maia, M. & Brunelli, D. The Eastern Romanche ridge-transform intersection (Equatorial Atlantic): slow spreading under extreme low mantle temperatures. Preliminary results of the SMARTIES cruise. in *EGU General Assembly Conference Abstracts* 10314 (2020). https://doi.org/10.5194/egusphere-egu2020-10314 (2020).
22. Maia, M., Brunelli, D. & Ligi, M. SMARTIES cruise, Pourquoi pas? R/V. (2019) https://doi.org/10.17600/18001107.
23. Havskov, J. & Ottemoller, L. SEISAN earthquake analysis software. *Seismol. Res. Lett.* **70**, 532–534 (1999).
24. Wang, Z., Singh, S. C., Prigent, C., Gregory, E. P. M. & Marjanović, M. Deep hydration and lithospheric thinning at oceanic transform plate boundaries. *Nat. Geosci.* **15**, 741–746 (2022).
25. Lomax, A., Virieux, J., Volant, P. & Berge-Thierry, C. Probabilistic earthquake location in 3D and layered models. In: *Advances in seismic event location* 101–134 (Springer, 2000).
26. Waldhauser, F. & Ellsworth, W. L. A double-difference earthquake location algorithm: method and application to the northern Hayward fault, California. *Bull. Seismol. Soc. Am.* **90**, 1353–1368 (2000).
27. Hardebeck, J. & Husen, S. Earthquake location accuracy. *CORSSA* 1–35 https://doi.org/10.5078/CORSSA-55815573. (2010)
28. Gomberg, J. S., Shedlock, K. M. & Roecker, S. W. The effect of *S* -wave arrival times on the accuracy of hypocenter estimation. *Bull. Seismol. Soc. Am.* **80**, 1605–1628 (1990).
29. Chatelain, J. L., Roecker, S. W., Hatzfeld, D. & Molnar, P. Microearthquake seismicity and fault plane solutions in the Hindu Kush Region and their tectonic implications. *J. Geophys. Res. Solid Earth* **85**, 1365–1387 (1980).
30. Bonatti, E. et al. Steady-state creation of crust-free lithosphere at cold spots in mid-ocean ridges. *Geology* **29**, 979–982 (2001).
31. Ligi, M., Bonatti, E., Cipriani, A. & Ottolini, L. Water-rich basalts at mid-ocean-ridge cold spots. *Nature* **434**, 66–69 (2005).
32. Wang, Z. & Singh, S. C. Seismic evidence for uniform crustal accretion along slow-spreading ridges in the equatorial Atlantic Ocean. *Nat. Commun.* **13**, 7809 (2022).
33. Schmid, F. & Schlindwein, V. Microearthquake activity, lithospheric structure, and deformation modes at an amagmatic ultraslow spreading Southwest Indian Ridge segment. *Geochem. Geophys. Geosyst.* **17**, 2905–2921 (2016).
34. Cannat, M. et al. Modes of seafloor generation at a melt-poor ultraslow-spreading ridge. *Geology* **34**, 605–608 (2006).
35. Müller, R. D., Sdrolias, M., Gaina, C. & Roest, W. R. Age, spreading rates, and spreading asymmetry of the world's ocean crust. *Geochem. Geophys. Geosyst.* **9**, Q04006 (2008).
36. Qin, Y., Singh, S. C., Grevemeyer, I., Marjanović, M. & Roger Buck, W. Discovery of flat seismic reflections in the mantle beneath the young Juan de Fuca Plate. *Nat. Commun.* **11**, 4122 (2020).
37. Molnar, P. The brittle-plastic transition, earthquakes, temperatures, and strain rates. *J. Geophys. Res. Solid Earth* **125**, e2019JB019335 (2020).
38. Chen, J., Crawford, W. C. & Cannat, M. Microseismicity and lithosphere thickness at a nearly-amagmatic oceanic detachment fault system. *Nat. Commun.* **14**, 430 (2023).
39. Key, J., White, R. S., Soosalu, H. & Jakobsdóttir, S. S. Multiple melt injection along a spreading segment at Askja, Iceland. *Geophys. Res. Lett.* **38**, L05301 (2011).
40. White, R. S., Edmonds, M., Maclennan, J., Greenfield, T. & Agustsdottir, T. Melt movement through the Icelandic crust. *Philos. Trans. R. Soc. Math. Phys. Eng. Sci.* **377**, 20180010 (2019).
41. Wright, T. J. et al. Geophysical constraints on the dynamics of spreading centres from rifting episodes on land. *Nat. Geosci.* **5**, 242–250 (2012).
42. Greenfield, T. & White, R. S. Building icelandic igneous crust by repeated melt injections. *J. Geophys. Res. Solid Earth* **120**, 7771–7788 (2015).
43. Greenfield, T. et al. Deep long period seismicity preceding and during the 2021 Fagradalsfjall eruption, Iceland. *Bull. Volcanol.* **84**, 101 (2022).
44. Flóvenz, Ó. G. et al. Cyclical geothermal unrest as a precursor to Iceland's 2021 Fagradalsfjall eruption. *Nat. Geosci.* **15**, 397–404 (2022).
45. Feuillet, N. et al. Birth of a large volcanic edifice offshore Mayotte via lithosphere-scale dyke intrusion. *Nat. Geosci.* **14**, 787–795 (2021).
46. Martens, H. R. & White, R. S. Triggering of microearthquakes in Iceland by volatiles released from a dyke intrusion. *Geophys. J. Int.* **194**, 1738–1754 (2013).
47. White, R. S. et al. Dynamics of dyke intrusion in the mid-crust of Iceland. *Earth Planet. Sci. Lett.* **304**, 300–312 (2011).
48. Dixon, J. E., Stoper, E. M. & Holloway, J. R. An experimental study of water and carbon dioxide solubilities in mid-ocean ridge basaltic

liquids. Part I: calibration and solubility models. *J. Petrol.* **36**, 1607–1631 (1995).
49. Kisslinger, C. A review of theories of mechanisms of induced seismicity. *Eng. Geol.* **10**, 85–98 (1976).
50. Hauri, E. H. et al. CO_2 content beneath northern Iceland and the variability of mantle carbon. *Geology* **46**, 55–58 (2018).
51. Le Voyer, M. et al. Carbon fluxes and primary magma CO_2 contents along the global mid-ocean ridge system. *Geochem. Geophys. Geosyst.* **20**, 1387–1424 (2019).
52. Le Voyer, M., Kelley, K. A., Cottrell, E. & Hauri, E. H. Heterogeneity in mantle carbon content from CO2-undersaturated basalts. *Nat. Commun.* **8**, 14062 (2017).
53. Saal, A. E., Hauri, E. H., Langmuir, C. H. & Perfit, M. R. Vapour undersaturation in primitive mid-ocean-ridge basalt and the volatile content of Earth's upper mantle. *Nature* **419**, 451–455 (2002).
54. Schilling, J.-G., Hanan, B. B., McCully, B., Kingsley, R. H. & Fontignie, D. Influence of the Sierra Leone mantle plume on the equatorial Mid-Atlantic ridge: a Nd-Sr-Pb isotopic study. *J. Geophys. Res. Solid Earth* **99**, 12005–12028 (1994).
55. Schilling, J.-G. et al. Thermal structure of the mantle beneath the equatorial Mid-Atlantic Ridge: Inferences from the spatial variation of dredged basalt glass compositions. *J. Geophys. Res. Solid Earth* **100**, 10057–10076 (1995).
56. Le Voyer, M., Cottrell, E., Kelley, K. A., Brounce, M. & Hauri, E. H. The effect of primary versus secondary processes on the volatile content of MORB glasses: an example from the equatorial Mid-Atlantic Ridge (5°N–3°S). *J. Geophys. Res. Solid Earth* **120**, 125–144 (2015).
57. Gale, A., Langmuir, C. H. & Dalton, C. A. The global systematics of ocean ridge basalts and their origin. *J. Petrol.* **55**, 1051–1082 (2014).
58. Eguchi, J. & Dasgupta, R. A CO2 solubility model for silicate melts from fluid saturation to graphite or diamond saturation. *Chem. Geol.* **487**, 23–38 (2018).
59. Shapiro, N. M. et al. Deep and shallow long-period volcanic seismicity linked by fluid-pressure transfer. *Nat. Geosci.* **10**, 442–445 (2017).
60. Wech, A. G., Thelen, W. A. & Thomas, A. M. Deep long-period earthquakes generated by second boiling beneath Mauna Kea volcano. *Science* **368**, 775–779 (2020).
61. Melnik, O., Lyakhovsky, V., Shapiro, N. M., Galina, N. & Bergal-Kuvikas, O. Deep long period volcanic earthquakes generated by degassing of volatile-rich basaltic magmas. *Nat. Commun.* **11**, 3918 (2020).
62. Korger, E. I. M. & Schlindwein, V. Seismicity and structure of the 85°E volcanic complex at the ultraslow spreading Gakkel Ridge from local earthquake tomography. *Geophys. J. Int.* **196**, 539–551 (2014).
63. Keller, T., Katz, R. F. & Hirschmann, M. M. Volatiles beneath mid-ocean ridges: deep melting, channelised transport, focusing, and metasomatism. *Earth Planet. Sci. Lett.* **464**, 55–68 (2017).
64. Audhkhasi, P. & Singh, S. C. Discovery of distinct lithosphere-asthenosphere boundary and the Gutenberg discontinuity in the Atlantic Ocean. *Sci. Adv.* **8**, eabn5404 (2022).
65. Mehouachi, F. & Singh, S. C. Water-rich sublithospheric melt channel in the equatorial Atlantic Ocean. *Nat. Geosci.* **11**, 65–69 (2018).
66. Kissling, E., Ellsworth, W. L., Eberhart-Phillips, D. & Kradolfer, U. Initial reference models in local earthquake tomography. *J. Geophys. Res. Solid Earth* **99**, 19635–19646 (1994).
67. Yu, Z., Singh, S. C. & Maia, M. Evidence for low Vp/Vs ratios along the eastern Romanche ridge-transform intersection in the equatorial Atlantic Ocean. *Earth Planet. Sci. Lett.* **621**, 118380 (2023).
68. Kissling, E. Geotomography with local earthquake data. *Rev. Geophys.* **26**, 659–698 (1988).
69. Christeson, G. L., Goff, J. A. & Reece, R. S. Synthesis of oceanic crustal structure from two-dimensional seismic profiles. *Rev. Geophys.* **57**, 504–529 (2019).
70. Hutton, L. & Boore, D. M. The ML scale in southern California. *Bull. Seismol. Soc. Am.* **77**, 2074–2094 (1987).
71. Wiemer, S. A software package to analyze seismicity: ZMAP. *Seismol. Res. Lett.* **72**, 373–382 (2001).
72. Hardebeck, J. L. & Shearer, P. M. A new method for determining first-motion focal mechanisms. *Bull. Seismol. Soc. Am.* **92**, 2264–2276 (2002).
73. Aupart, C., Schlindwein, V., Ben-Zion, Y., Renard, F. & Jamtveit, B. Seismic Controls on the Progress of Serpentinization at Ultra-Slow Spreading Ridges. http://www.essoar.org/doi/10.1002/essoar.10502242.1 (2020).
74. Meier, M. et al. Segment-scale seismicity of the ultraslow spreading Knipovich Ridge. *Geochem. Geophys. Geosyst.* **22**, e2020GC009375 (2021).
75. Lehnert, K., Su, Y., Langmuir, C. H., Sarbas, B. & Nohl, U. A global geochemical database structure for rocks. *Geochem. Geophys. Geosyst.* **1** https://doi.org/10.1029/1999GC000026 (2000).
76. Iacono-Marziano, G., Morizet, Y., Le Trong, E. & Gaillard, F. New experimental data and semi-empirical parameterization of H2O–CO2 solubility in mafic melts. *Geochim. Cosmochim. Acta* **97**, 1–23 (2012).
77. Wessel, P. et al. The generic mapping tools version 6. *Geochem. Geophys. Geosyst.* **20**, 5556–5564 (2019).
78. Hicks, S. P. et al. Back-propagating supershear rupture in the 2016 M_w 7.1 Romanche transform fault earthquake. *Nat. Geosci.* **13**, 647–653 (2020).
79. Cartigny, P., Pineau, F., Aubaud, C. & Javoy, M. Towards a consistent mantle carbon flux estimate: Insights from volatile systematics (H_2O/Ce, δD, CO_2/Nb) in the North Atlantic mantle (14°N and 34°N). *Earth Planet. Sci. Lett.* **265**, 672–685 (2008).

Acknowledgements

We are grateful to the officers, crew, and scientific party for their hard work during the 2019 SMARTIES cruise. We thank P. Cartigny, L. Geli, Z. Wang, and A.Y. Yang for the useful discussions. Z.Y. is partly funded by the National Natural Science Foundation of China (42422603, 42330308) and the Zhejiang Provincial Natural Science Foundation of China (No. LDQ24D060001). This research was funded by the ISblue project, the Interdisciplinary graduate school for the blue planet (ANR-–17-EURE-0015), the French government under the program "Investissements d'Avenir", the Regional Council of Brittany (SAD program), the European Research Council under the European Union's Seventh Framework Program (FP7/2007–2013) to S.C.S, and the ERC Advanced Grant agreement no. 339442_TransAtlanticILAB to S.C.S. The shipping time for the SMARTIES cruise was funded through the TGIR French Oceanographic Fleet. This work is IPGP contribution no. 4293.

Author contributions

Z.Y. processed the microseismicity data, analyzed the results, and wrote the paper. S.C.S. supervised the data acquisition, data processing, and interpretation of the seismic data, developed the idea, and wrote the paper. C.H. and L.G. collected the available geochemical data and analyzed them. C.H. performed geochemical interpretation and calculation. M.M., A.B., and L.P. performed structural analysis. M.M. and D.B. designed the SMARTIES project. M.M., D.B., A.B., and L.P. participated in the data collection during the SMARTIES cruise. All authors discussed the results and commented on the manuscript.

Competing interests

The authors declare no competing interests.

Additional information

Supplementary information The online version contains supplementary material available at https://doi.org/10.1038/s41467-024-55792-9.

Correspondence and requests for materials should be addressed to Zhiteng Yu or Satish C. Singh.

Peer review information *Nature Communications* thanks the anonymous, reviewers for their contribution to the peer review of this work. A peer review file is available.